



Metal-organic framework derived FeS/MoS₂ composite as a high performance anode for sodium-ion batteries



Likang Fu^a, Wenqi Xiong^a, Qiming Liu^{a,*}, Shuyun Wan^a, Chenxia Kang^a, Gaofeng Li^b, Jun Chu^b, Yucheng Chen^a, Shengjun Yuan^{a,*}

^a School of Physics and Technology, Key Laboratory of Artificial Micro, and Nano-structures of Ministry of Education, Wuhan University, Wuhan 430072, China

^b College of Chemistry and Molecular Sciences, Wuhan University, Wuhan 430072, China

ARTICLE INFO

Article history:

Received 3 January 2021

Received in revised form 23 February 2021

Accepted 25 February 2021

Available online 3 March 2021

Keywords:

Metal organic framework

FeS/MoS₂

Flower-like

Adsorption energy

Density functional theory

Sodium ion batteries

ABSTRACT

Considering the superior performances of MOF-based and MoS₂-based materials, a flower-like FeS/MoS₂ composite is synthesized using MIL-100(Fe) as a precursor. Electronic density of states and band structure are simulated by density functional theory (DFT) calculations, which prove that FeS/MoS₂ heterostructure exhibits metallic behavior. Unique structure and powerful hetero-interface synergistic effect of FeS/MoS₂ is conducive to improve the stability of sodium-ion batteries (SIBs). It provides reversible capacities of 464 and 365 mA h g⁻¹ at 0.1 and 1.0 A g⁻¹. When the current density increases to 5 A g⁻¹, FeS/MoS₂ delivers a high capacity of 325 mA h g⁻¹ with a capacity retention rate (71.1%). Moreover, it can maintain a stable specific capacity of 331 mA h g⁻¹ at 2.0 A g⁻¹ after 200 cycles. Adsorption energy calculated by DFT indicates that more Na atoms may be trapped on the top of Mo atom between FeS and MoS₂ layers. This study may stimulate the interesting of multivariate-MOFs/ covalent organic frameworks (COFs) composite emerging two-dimensional materials and facilitate the application of composite electrode in high-performance SIBs.

© 2021 Elsevier B.V. All rights reserved.

1. Introduction

With the increasing consumption of fuels resources and demand of energy security, the sustainable energy storage technologies highlight the importance in the realm of electrical energy [1–3]. Lithium ion batteries (LIBs) are applied in electronic products and new energy vehicle largely, owing to the advantages of high energy density and long lifetime [4–6]. The limited and expensive lithium resources make the suitable alternatives of LIBs stand out [7,8]. Remarkably, sodium ion batteries (SIBs) have been regarded as the possible substitute for LIBs because of the similar storage mechanism (insertion, conversion and alloying). It also has caught increasing attention in terms of large-scale energy storage depending on abundant resources, low cost and environmental friendliness [9–12]. Nevertheless, there are still some bottleneck problems for SIBs before further commercialization [13,14]. For example, the reversible capacity and cycle stability are seriously affected by the high molar mass and large ionic radius of sodium. Compared with LIBs, graphite cannot be employed as commercial electrode in SIBs because of the sodium ionic diameter (Na 1.02 Å vs. Li 0.76 Å) [15].

Moreover, electrode materials of SIBs are also restricted by the high ionization potential [16]. The key to improve the electrode performance is to choose the appropriate materials and carry out reasonable design or modification, so as to achieve the effects of excellent cycling performance and rate capability. To date, various alternative electrode materials, such as Prussian blue analogs [17,18], alloy compound [19,20], metal oxides and sulfides [21–23], carbon/phosphorus-based materials [24,25], have been synthesized and proved to possess good potential value.

Metal-organic frameworks (MOFs) have attracted great research interests in various fields because of their designable framework structure, high surface area, adjustable shape and porosity [26–32]. In general, energy storage electrode materials with hollow, core-shell and hetero-junction nanostructures can be easily prepared using MOFs as precursor [33,34]. For one thing the MOF-derived nanoporous can improve diffusion kinetics of sodium ion and relieve the electrode deformation during the process of Na⁺ intercalation/de-intercalation. For another the carbon formed in situ by organic ligands can enhance the conductivity of electrode materials, creating an increase of the charge transfer efficiency. Pan et al. proposed a strategy using Cu-based MOFs as reactant template to fabricate porous hollow octahedron CuO/Cu₂O, which delivers a steady capacity of 415 mA h g⁻¹ at 0.05 A g⁻¹ [35]. Yang et al. synthesized a NHPCS active material and showed a specific capacity of

* Corresponding authors.

E-mail addresses: qmliu@whu.edu.cn (Q. Liu), s.yuan@whu.edu.cn (S. Yuan).

291 mA h g⁻¹ at 0.2 A g⁻¹ [36]. Zhu et al. fabricated a Ni₃S₂/Co₉S₈/N-doped carbon electrode using Ni-Co-MOF as precursor, exhibiting reversible specific capacities of 419.9 and 323.2 mA h g⁻¹ at 0.1 and 2.0 A g⁻¹ [37]. In addition to the above transition-metal dichalcogenides (TMDCs), MoS₂-based materials can be also used as the electrodes of SIBs. They possess graphite-like layered structure and high reversible capacity [38–41]. Considering the special properties of MOFs and two-dimensional materials, their composites will have certain research significance in SIBs.

Herein, we first reported a convenient strategy of the synthesis of FeS/MoS₂ composite via post-sulfuration of MIL-100(Fe) without the utilization of sulfur powder. The interfacial interaction between MoS₂ and FeS is beneficial to capture polysulfide intermediate and relieve the volume deformation of FeS/MoS₂ electrode. The charge transfer rate of sodium ion is accelerated because of interfacial electric field. FeS/MoS₂ anode material exhibits stable specific capacities of 464 and 365 mA h g⁻¹ at 0.1 and 1.0 A g⁻¹. Besides, after 200 cycles, FeS/MoS₂ also delivers a specific capacity of 331 mA h g⁻¹ at 2.0 A g⁻¹. It is shown through comparison experiments that the cycling and rate capacities of FeS/MoS₂ are much higher than those of FeS/FeS₂ and MoS₂. This design concept of using the Fe-MOF as a template to composite 2D materials may provide a wide application prospect for the development of high performance SIBs.

2. Experimental section

2.1. Materials

Trimesic acid (98%) and ammonium tetrathiomolybdate (99.97%) were purchased from Shanghai Aladdin Bio-Chem Technology Co., Ltd. Iron(III) nitrate nonahydrate (≥ 98.5%), ethanol (≥ 99.7%), thioacetamide (≥ 99%), metallic sodium (99.7%) and N,N-Dimethylformamide (DMF, ≥ 99.5%) were ordered from Sinopharm Chemical Reagent Co., Ltd. Carbon black (Super P), glass fiber (Whatman, GF/A), CR-2032 cell shell, polyvinylidene fluoride (PVDF), N-methyl-2-pyrrolidone (NMP) and Cu foil were purchased from Guangdong Canrd New Energy Technology Co., Ltd. NaClO₄ electrolyte, fluoroethylene carbonate (FEC), dimethyl carbonate (DMC) and ethylene carbonate (EC) were ordered from DoDo Chemical Technology Co., Ltd.

2.2. Preparation of MIL-100(Fe) and Fe₃C precursor

The MIL-100(Fe) was synthesized using a method described in Ref. [42]. Iron(III) nitrate nonahydrate (0.056 mol) and trimesic acid (H₃BTC, 0.038 mol) were mixed with deionized (DI) water (56 mL) and stirred for 2 h. The above mixture was put in a sealed autoclave after complete dissolution, reacting at 160 °C for 15 h. The precipitate was washed with DI water/ethanol and collected by centrifuging. The MIL-100(Fe) was obtained after drying at 80 °C for 24 h. The Fe₃C precursor was produced by a calcination treatment of MIL-100(Fe) at 700 °C in argon atmosphere for 2 h.

2.3. Preparation of FeS/MoS₂ composite

The FeS/MoS₂ composite was prepared via a solvothermal method [43]. Fe₃C precursor (60 mg) and ammonium tetrathiomolybdate ((NH₄)₂MoS₄, 0.46 mmol) were added in the mixed solvents of DMF (50 mL) and ethanol (10 mL). After ultrasonic treatment and uniform stirring, the mixture was reacted at 200 °C for 24 h. The precipitate was washed with DMF/ethanol and dried in vacuum at 65 °C for 12 h. The target product (FeS/MoS₂) was got by a heat treatment at 300 °C with a heating rate of 2 °C min⁻¹ for 2 h. Additionally, pure MoS₂ and FeS/FeS₂ were prepared by the same process using (NH₄)₂MoS₄ and Fe₃C precursor/thioacetamide, respectively.

2.4. Materials characterization

The phases and elemental analysis of FeS/MoS₂, FeS/FeS₂ and MoS₂ were detected by X-ray diffraction (D8 ADVANCE, Bruker) and X-ray photoelectron spectroscopy (XPS, ESCALAB 250X, Thermo Fisher Scientific). Morphology and lattice fringe spacing were observed by a field emission scanning electron microscopy (FESEM, ZEISS Sigma) and transmission electron microscopy (TEM, JEM-2100 microscope, JOEL). The porosity and specific area were measured by an automated adsorption apparatus (JW-BK 100B) at 77 K using the BJH and Brunauer-Emmett-Teller (BET) methods.

2.5. Electrochemical measurements

The electrochemical properties of electrodes were tested with half-cells (CR2032), which assembled at a glove-box of high purity Ar atmosphere. The electrodes were prepared as follows: FeS/MoS₂, Super P and PVDF (60:30:10) were mixed with NMP to form the slurry and coat on pure Cu foil. Coated foil was dried at 90 °C in vacuum for 8 h. The obtained working electrode was cut into discs with a diameter of 12 mm. The mass range of active substances is about 1.2–1.8 mg. Glass fiber (Whatman, GF/A) was used as the separator. Metallic sodium was used as counter electrode for SIBs. 1.0 M NaClO₄ dissolved in EC/DMC with FEC (5 wt%) was used as electrolyte. CHI 760E electrochemical workstation was applied for measuring cyclic voltammetry (CV) plots. The galvanostatic charge/discharge tests for sodium storage were detected by a LANHE CT2001A instrument within a work voltage range of 0.01–3.0 V.

2.6. Density functional theory (DFT) calculation

In order to determine the bind ability between Na⁺ and anode material, the density functional theory (DFT) calculations were performed by a VASP package. The electron/ion potential was analyzed with projected augmented wave (PAW) and the exchange-correlation functional was discussed by generalized gradient approximation (GGA) [44]. The geometric structures of FeS and MoS₂ were optimized by the k-point meshes of 4 × 4 × 2 and 15 × 15 × 1 [45]. The kinetic energy cut-off, energy convergence and stress force criterions were set as 500 eV, 10⁻⁵ eV and 0.01 eV Å⁻¹. The van der Waals interaction force was analyzed with a semi-empirical DFT-D3 method [46,47]. The relaxed lattice parameters of FeS (MoS₂) were a = b = 5.706 Å, c = 10.346 Å (a = b = 3.183 Å). When constructing a heterobilayer, a 5 × 5 MoS₂ and a 3 × 3 FeS were used. The adsorption energy (E_{ads}) of the Na atom on FeS/MoS₂ can be defined as follows:

$$E_{\text{ads}} = E_{\text{bilayer+Na}} - E_{\text{bilayer}} - E_{\text{Na}}$$

where E_{bilayer+Na} and E_{bilayer} are the total energy of heterobilayer with and without Na atom respectively, E_{Na} is the energy of an isolated Na atom.

3. Results and discussion

The flower-like FeS/MoS₂ was prepared via solvothermal reaction and calcination using MIL-100(Fe) as a precursor, of which the schematic diagram was illustrated in Fig. 1. MIL-100(Fe) was firstly prepared by a hydrothermal method and calcined at 700 °C for 2 h under the protection of Ar, producing Fe₃C (Fig. S1). After the solvothermal sulfurization with (NH₄)₂MoS₄ and calcination in argon atmosphere, the final product FeS/MoS₂ was gained.

The morphology of FeS/MoS₂ was systematically characterized by FESEM and TEM (Fig. 2). As exhibited in Fig. 2a, the FESEM images of FeS/MoS₂ composite reveal a flower-like structure, which is synthesized with the calcined MIL-100(Fe) as a template (Fe₃C). Comparing the FESEM images of MIL-100(Fe) and Fe₃C presented in Fig. S2, it is clear that the surfaces of as-prepared MOFs become rougher and even

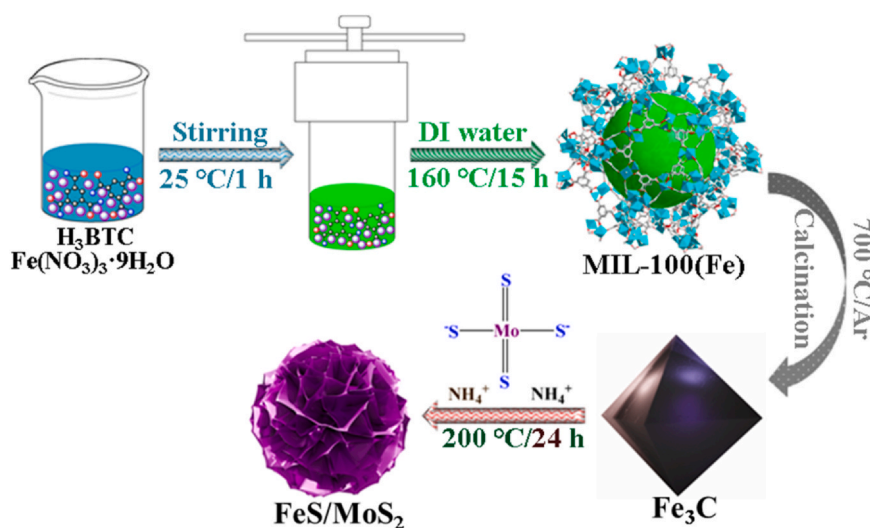


Fig. 1. Schematic illustration of preparation procedure of flower-like FeS/MoS₂.

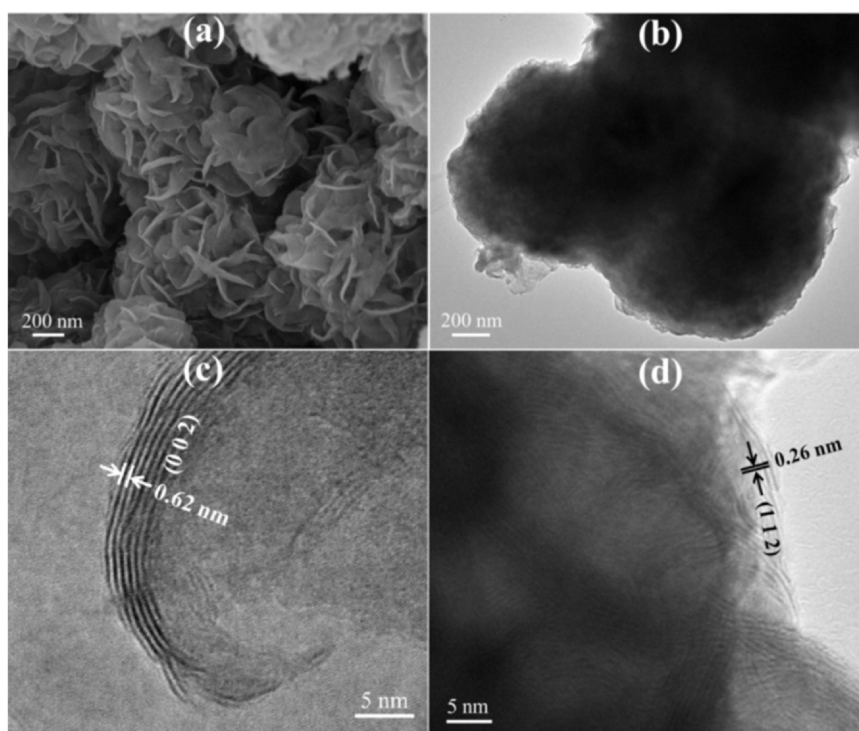


Fig. 2. FESEM images (a), TEM images (b) and high-resolution TEM images (c) of the FeS/MoS₂ composite.

appear some flaws after calcination treatment. The roughness and flaws changes of MOFs template are conducive to the formation and growth of FeS/MoS₂ composite. The energy-dispersive spectroscopy (EDS) elemental mapping images of FeS/MoS₂ are presented in Fig. S3a–e, which indicate that the Fe, S, Mo and C elements exist in the above as-prepared composite. In terms of structure and size of the as-synthesized material, the results of TEM images and above FESEM images are in good agreement. As displayed in Fig. 2b, the internal structure of FeS/MoS₂ is relatively compact rather than a core-shell structure. This structure will result in a low initial coulomb efficiency and a slow rising trend of the specific capacity, which is consistent with the actual results using FeS/MoS₂ as anode for SIBs. The high-resolution TEM (HRTEM) images of FeS/MoS₂ are shown in Fig. 2c–d. The lattice fringe spacing of 0.62 nm is consistent with the (0 0 2)

plane of MoS₂ phase and the lattice fringe spacing measured to be 0.26 nm corresponds to the (1 1 2) plane of FeS phase. Furthermore, FeS and MoS₂ phases are proofed with selected-area electron diffraction (Fig. S3f). The diffraction rings correspond to the (3 0 0), (1 1 4) and (1 0 0) planes of FeS and MoS₂ respectively. These results show that the flower-like FeS/MoS₂ composite has been synthesized successfully.

The phases of the as-prepared samples were studied by XRD (Fig. 3). There are three diffraction peaks around at 14.4°, 32.7° and 58.3° in the pattern of MoS₂, which correspond to (0 0 2), (1 0 0) and (1 1 0) planes of the MoS₂ (JCPDS No.87-2416). For the pattern of FeS/FeS₂, some diffraction peaks around 29.9°, 33.9°, 43.9°, 53.1° and 28.5°, 33.1°, 37.1°, 40.8°, 47.4°, 56.3°, corresponding to (1 1 0), (1 1 2), (1 1 4), (3 0 0) and (1 1 1), (2 0 0), (2 1 0), (2 1 1), (2 2 0), (3 1 1) planes

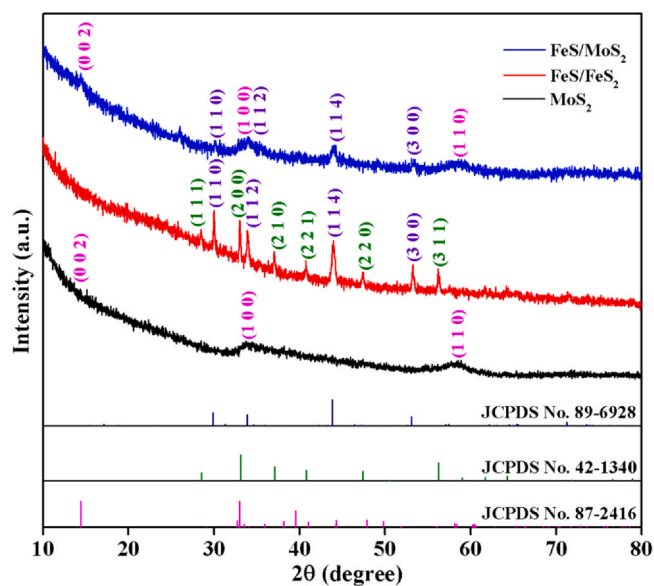


Fig. 3. XRD patterns of the FeS/MoS₂, FeS/FeS₂ and MoS₂.

of FeS (JCPDS No.89-6928) and FeS₂ (JCPDS No.42-1340). In the XRD pattern of FeS/MoS₂, there are a series of diffraction peaks at 29.9°, 33.9°, 43.9°, 53.1° and 14.4°, 32.7°, 58.3°, which are corresponded to (1 1 0), (1 1 2), (1 1 4), (3 0 0) and (0 0 2), (1 0 0), (1 1 0) planes of FeS (JCPDS No.89-6928) and MoS₂ (JCPDS No.87-2416). XRD pattern verifies the results of TEM images, showing that MoS₂, FeS/FeS₂ and FeS/MoS₂ have been prepared. The nitrogen adsorption-desorption isotherms of FeS/MoS₂ composite is illustrated in Fig. S4, getting the BET specific surface area of 16.46 m²/g and pore volume of 0.13 cm³/g. The result indicates that FeS/MoS₂ composite can provide sufficient active sites for contacting with the electrolyte when it is applied as an electrode in SIBs.

Elemental composition and oxidation states of the FeS/MoS₂ were investigated by XPS. Four elements of Fe, Mo, S and C in the FeS/MoS₂ composite were confirmed according to the survey spectrum (Fig. S5). As presented in Fig. 4a, the spectrum of Fe 2p can be divided into three characteristic peaks. The peaks at 711.5, 724.9 and 721.5 eV correspond to the characteristic peaks of Fe²⁺ 2p_{3/2}, Fe²⁺ 2p_{1/2} and satellite in FeS, respectively [48–50]. For the spectrum of Mo 3d, there are two groups of peaks around at 231.8, 228.5 eV and 233.2, 229.6 eV, belonging to 1T-MoS₂ and 2H-MoS₂ [51]. In Fig. 4b, there are four characteristic peaks at 226.7, 229.6, 232.7 and 236.1 eV, which correspond to S 2s, Mo⁴⁺ 3d_{5/2}, Mo⁴⁺ 3d_{3/2} and

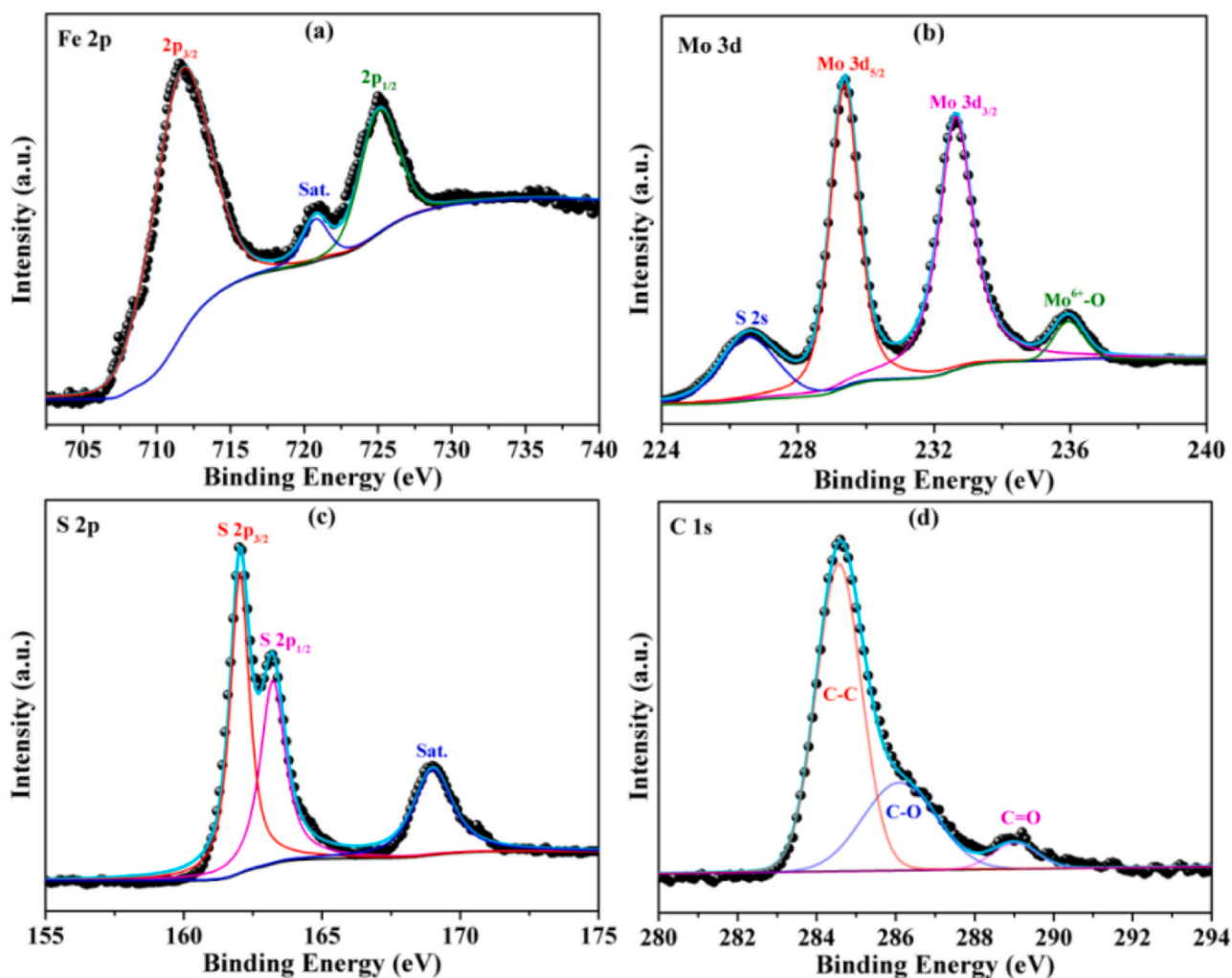


Fig. 4. High-resolution XPS spectra of FeS/MoS₂, (a) Fe 2p spectrum, (b) Mo 3d spectrum, (c) S 2p spectrum and (d) C 1s spectrum.

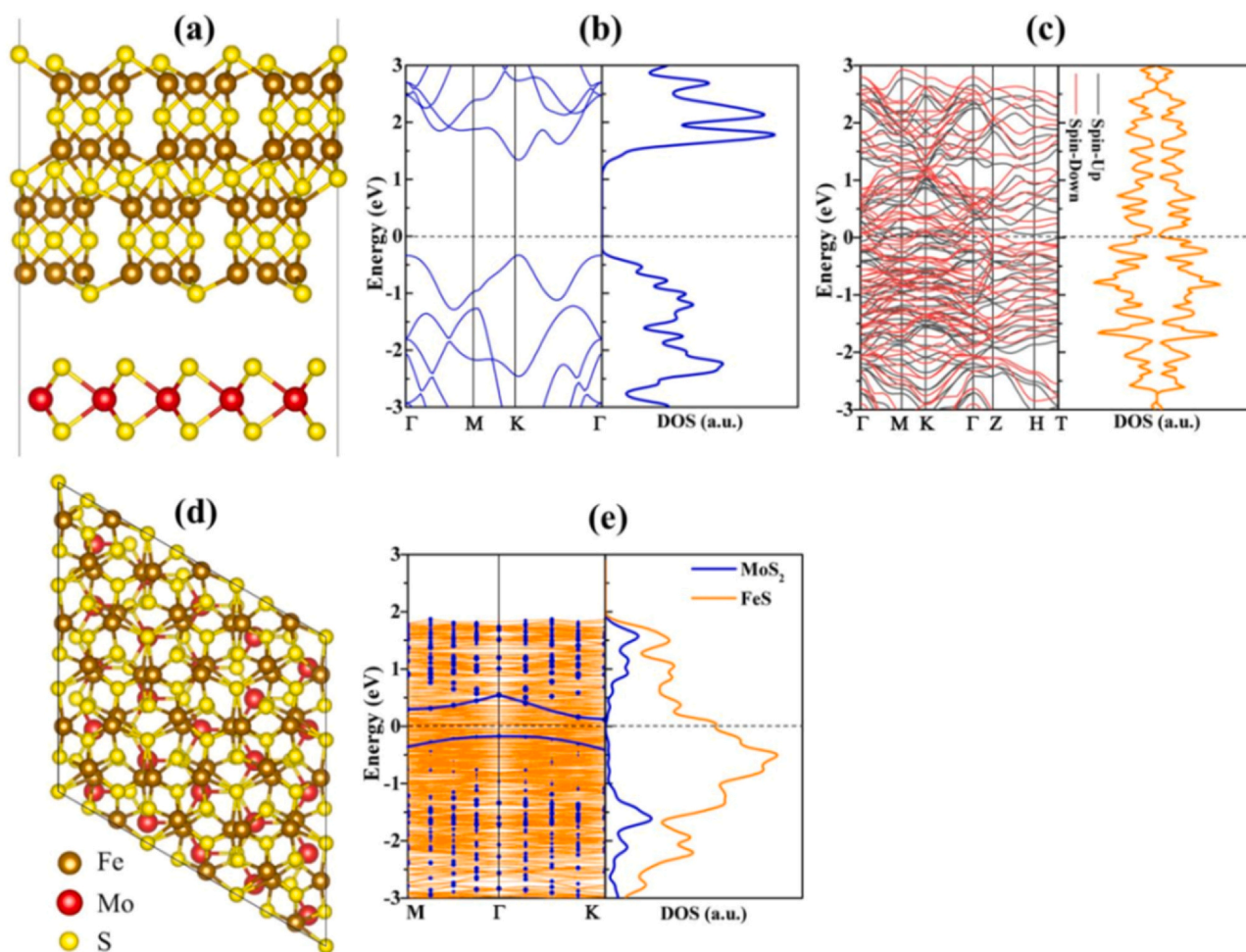


Fig. 5. (a) Geometric models of MoS₂ and FeS, (b–c) band structure and electronic density of states (DOS) of MoS₂ and FeS, (d) crystal model, (e) band structure and electronic density of states (DOS) of FeS/MoS₂.

Mo⁶⁺-O, respectively [51,52]. The reason for Mo⁶⁺-O is that the FeS/MoS₂ composite is partially oxidized in air before XPS detection. For the S 2p spectrum (Fig. 4c), the characteristic peaks located at 162 and 163.2 eV are separately assigned to S 2p_{3/2} and S 2p_{1/2}, indicating that sulfur is as S²⁻ states in FeS and MoS₂ [52,53]. In addition, the characteristic peak at 168.5 eV corresponds to a satellite peak of sulfur (polysulfide or oxidized group). The spectrum of C 1s, as depicted in Fig. 4d, is fitted as three peaks. The characteristic peaks at 284.6, 286.4 and 289.2 eV are assigned to C–C, C–O and C=O bonds [54,55]. Oxygen-containing groups in the FeS/MoS₂ composite are derived from the partial oxidation and thermal decomposition of the samples [48]. The valence and bonds of all the elements in FeS/MoS₂ composite have been verified by the XPS analysis.

The diffusion dynamics of hetero-interfaces between FeS and MoS₂ were analyzed by density functional theory (DFT) calculations (Fig. 5). The geometric models of single FeS, MoS₂ and FeS/MoS₂ heterostructure are exhibited in Fig. 5a and d. With the generation of the heterojunction in the interfaces of FeS and MoS₂ and the introduction of electric field, the charge transfer rate of Na⁺ will be accelerated [56–58]. As depicted in Fig. 5b–c and e, there are great differences in electronic DOS and band structure of MoS₂, FeS and FeS/MoS₂. These results manifest that the primary band-gap of MoS₂ is greatly reduced when it is compounded with FeS. The FeS/MoS₂ heterostructure exhibits metallic behaviour, indicating that ionic/electronic conductivity at the heterogeneous interface is higher, which is more conducive to the kinetics of Na-ion diffusion [56,59].

In the light of the above structure characterization and element component results, the as-formed FeS/MoS₂ can afford to be a proper anode material for SIBs. The electrochemical behaviors were firstly researched by cyclic voltammetry (CV) method. Fig. 6a demonstrates the CV curves of FeS/MoS₂ composite electrode for four consecutive cycles tested at 0.1 mV s⁻¹ within a voltage range of 0.01–3.0 V (vs. Na⁺/Na). There are five peaks at 0.15, 0.3, 0.62, 0.87 and 1.5 V in the first cathodic scan. The peaks around at 1.5, 0.87 and 0.3 V are associated with the electrochemical reduction between Na⁺ and FeS to form Na₂FeS₂, Na₂S and Fe, along with the solid electrolyte interface (SEI) films formation [48,49,60]. Two cathodic peaks around at 0.62 and 0.15 V are related to the insertion of Na⁺ into MoS₂ to form Na_xMoS₂, Na_xS, Na₂S and Mo [16,39,61]. During the anodic scan process, five oxidation peaks are observed and located at 0.49, 0.73, 1.34, 1.77 and 2.14 V. Two peaks appear at 0.73 and 1.77 V, which are because of the oxidation of Mo from zero-valent to Mo⁴⁺/Mo⁶⁺ [62,63]. The oxidation peaks around at 0.49, 1.34 and 2.14 V are attributed to the transition of Fe and Na₂S to Na₂FeS₂ and Na_xFeS phases during the desodiation process [49,64]. For the second scan process, the cathodic peaks are located at 0.11, 0.66, 1.29 and 2.25 V, which are different from the peaks in the first cathodic process. The reason can be attributed to the final product after first cycle is Na_{2-x}FeS₂ rather than the original FeS [65–67]. For the anodic process, the corresponding oxidation peaks are also shifted slightly. Compared with the second cycle, there is a voltage deviation in the cathodic peak of the third cycle at low potential, which is assigned to the effect of Na_{2-x}FeS₂ on the insertion reaction between Na⁺ and

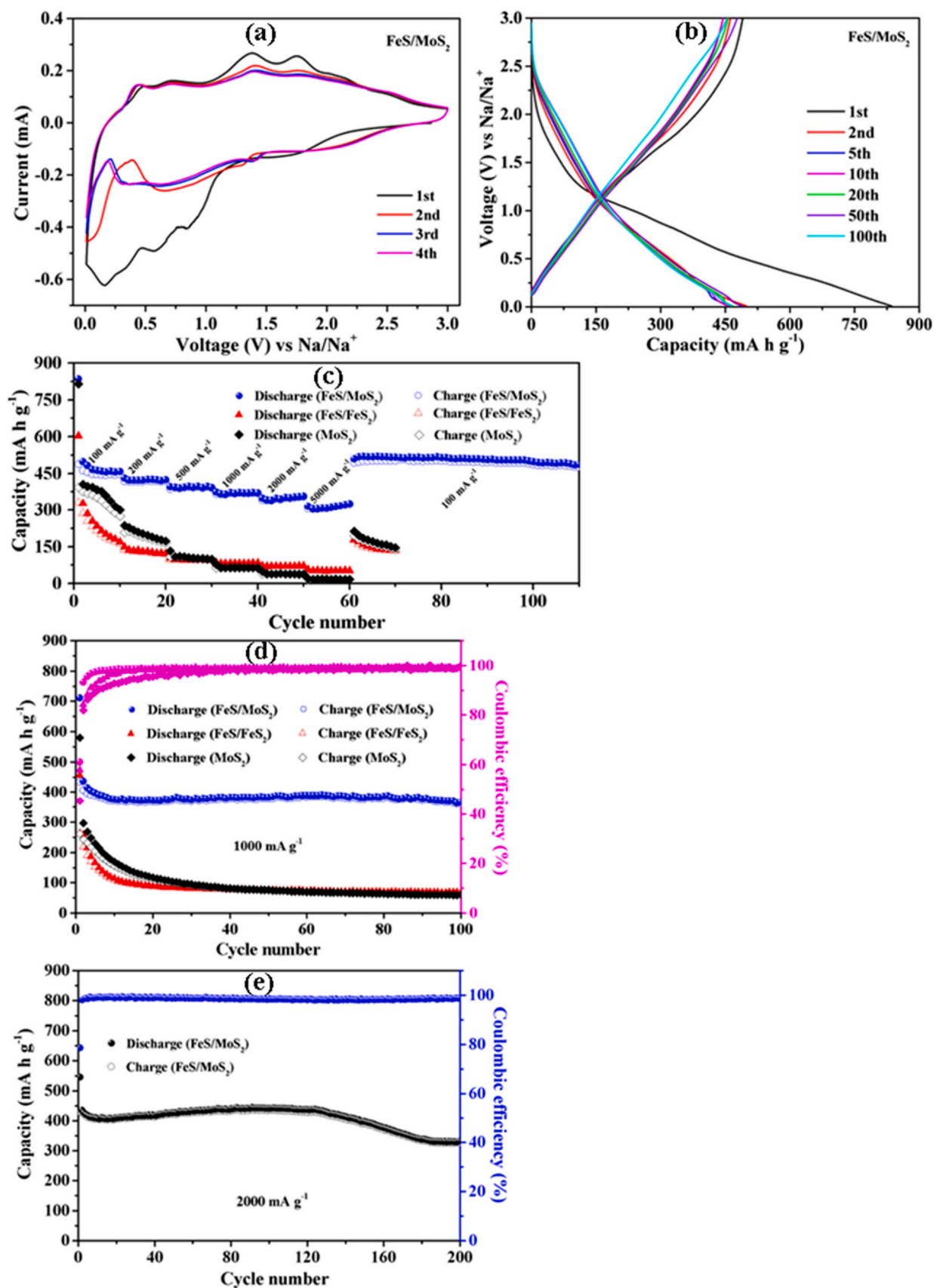


Fig. 6. (a) CV curves of FeS/MoS₂ at 0.1 mV s⁻¹ and (b) discharge/charge curves at 0.1 A g⁻¹, (c) rate capability of FeS/MoS₂, FeS/FeS₂ and MoS₂ and (d) cycling performance at 1.0 A g⁻¹, (e) cycling performance of FeS/MoS₂ at 2.0 A g⁻¹.

Table 1
Summary of the electrochemical performances of FeS and MoS₂ as anodes for SIBs.

Material structure	Specific capacity (mA h g ⁻¹)	Current density (mA g ⁻¹)	Cycling number
FeS@C-N [72]	354.5	100	500
FeS/ZnS [73]	475.1	100	50
CL-C/FeS [74]	260	1000	200
G-MoS ₂ [75]	175	2000	400
N-doped MoS ₂ /C [76]	128	2000	5000
This work	331	2000	200

MoS₂. The subsequent CV curves are almost overlapped, suggesting that FeS/MoS₂ electrode has high reversibility and stability in SIBs.

Galvanostatic discharge/charge curves of FeS/MoS₂ for the 1st, 2nd, 5th, 10th, 20th, 50th and 100th cycles are presented in Fig. 6b, and the slopes match well with the results of CV curves. When discharge and charge at 0.1 A g⁻¹, FeS/MoS₂ composite delivers initial discharge and charge capacities of 835 and 495 mA h g⁻¹, respectively, corresponding to a Coulombic efficiency (CE) of 59.3%. In the initial cycle, the capacity loss is caused by the electrolyte decomposition and SEI layer formation [68,69]. In the subsequent cycles, there is no discrepancy in the discharge and charge curves. The reversible discharge capacities for the 2nd, 5th, 10th, 50th and 100th cycles are 499, 462, 457, 467, 489 and 464 mA h g⁻¹ with a CEs of ~98%, manifesting that FeS/MoS₂ electrode delivers stable capacities in SIBs.

The rate capabilities of FeS/MoS₂, FeS/FeS₂ and MoS₂ electrodes were assessed at 0.1, 0.2, 0.5, 1.0, 2.0 and 5.0 A g⁻¹, as depicted in Fig. 6c. The reversible capacities of FeS/MoS₂ are 457, 424, 393, 371, 356 and 325 mA h g⁻¹ at 0.1, 0.2, 0.5, 1.0, 2.0 and 5.0 A g⁻¹ with capacity retention rates of 100%, 92.7%, 86.0%, 81.1%, 77.9% and 71.1% respectively, which are much greater than those values of the FeS/FeS₂ and MoS₂ (Fig. S6). When the current density returns from 5.0 to 0.1 A g⁻¹, the discharge capacity is still up to 509 mA h g⁻¹ and then stable at 487 mA h g⁻¹ after 50 cycles, indicating that as-made FeS/MoS₂ composite has a high sustainability. In contrast, the FeS/FeS₂ and MoS₂ electrodes show pretty poor rate capability. Reversible capacities and capacity retention rates of FeS/FeS₂ and MoS₂ are 52 mA h g⁻¹, 17 mA h g⁻¹ and 30.6%, 5.6% at 5.0 A g⁻¹. Also, the cycling performance of the FeS/MoS₂, FeS/FeS₂ and MoS₂ electrodes were tested and contrasted at 1.0 A g⁻¹ (Fig. 6d). For the FeS/MoS₂ composite anode, the initial discharge and charge capacities are 711 and 435 mA h g⁻¹ at 1.0 A g⁻¹, leading to a CE of 61.1%.

The discharge capacity is 365 mA h g⁻¹ with the CE up to 99% after 100 cycles. For the FeS/FeS₂ and MoS₂ anodes, the discharge/charge capacities are 465/264 mA h g⁻¹ and 580/262 mA h g⁻¹ at the same cycle conditions and the retention rates are only 14.7% and 10.3%. These results prove that FeS/MoS₂ composite anode has a great advantage in rate capability and cycling performance over FeS/FeS₂ and MoS₂. Besides that, the cycling performance of FeS/MoS₂ electrode was further studied at a large current density (Fig. 6e). After 200 cycles, it delivers a high reversible capacity of 331 mA h g⁻¹ at 2.0 A g⁻¹ and the capacity retention rate is up to 78% in contrast with the 2nd cycle. The outstanding cycling and rate capabilities of as-synthesized FeS/MoS₂ composite demonstrate that the activation energy and Ohmic resistance of sodium ion diffusion are reduced after combining with MoS₂, which result in the speedy Faraday effects. The reason can be summed up that short paths, open structure and large amounts of ion insertion channels promote the rapid diffusion of sodium ion [43,70,71]. The cyclic performance of FeS/MoS₂ composite as an anode for SIBs is compared to the reported FeS and MoS₂ materials, as listed in Table 1. Most of reported FeS and MoS₂ electrode materials are limited to current density of less than 1000 mA g⁻¹ or low cycle numbers. For the FeS/MoS₂ composite anode, it can deliver an excellent cycling capacity (331 mA h g⁻¹) even at a large current density (2000 mA g⁻¹).

In order to more clearly understand the sodium storage performance of the above materials, electrochemical impedance spectroscopy (EIS) spectra for the FeS/MoS₂, FeS/FeS₂ and MoS₂ electrodes were performed at the open circuit potential. As displayed in Fig. 7, all Nyquist plots show oblique lines at low frequency area and compressive semi-circles at high frequency area, corresponding to the Warburg impedance associated with Na⁺ diffusion and the charge transfer resistance (R_{ct}) at the electrode and electrolyte interface, respectively [77]. The corresponding resistance values were gained by the simulation of testing data with the equivalent circuit model. Obviously, the R_{ct} of FeS/MoS₂ composite electrode is 53.2 Ω , which is smaller than those of FeS/FeS₂ (95.1 Ω) and MoS₂ (99.8 Ω). The results imply that the electrochemical reaction rate and electrical conductivity of FeS/MoS₂ composite are superior to the other two electrodes (Fig. 7a) [78]. As the number of cycles increases, the R_{ct} value of FeS/MoS₂ electrode is decreased and then stable at 42.5 Ω after the 100th cycle (Fig. 7b), which shows a good cycling stability in sodium-ion storage.

To deeply comprehend the effect of FeS/MoS₂ composite hetero-bilayer on the electrochemical performance of sodium ion storage, DFT calculations were performed by VASP package to investigate adsorption behavior of Na on FeS/MoS₂ hetero-bilayer.

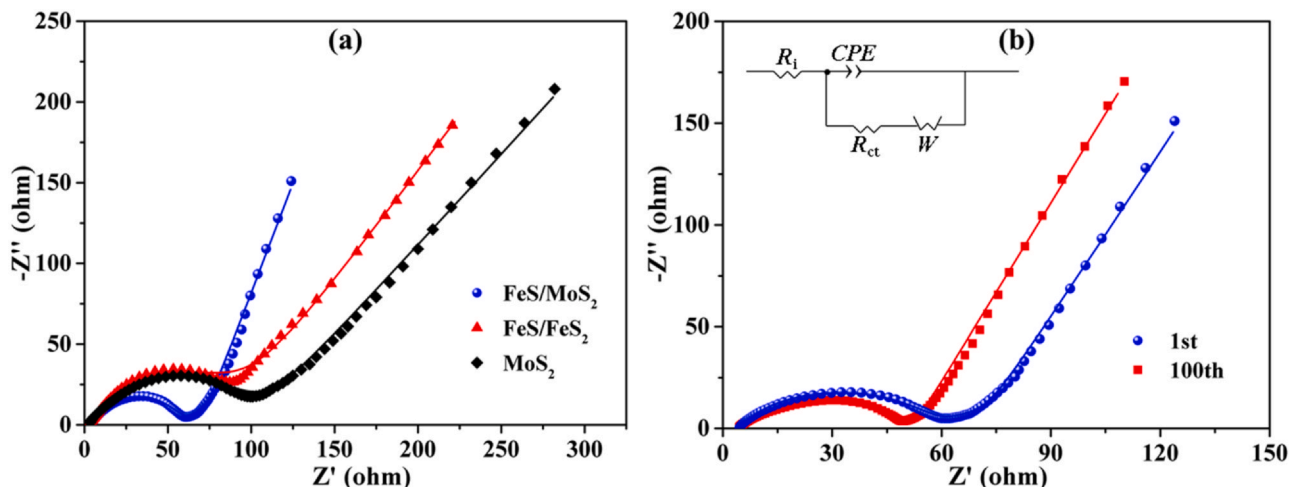


Fig. 7. Nyquist plots of (a) three different electrodes after one cycle, (b) the FeS/MoS₂ electrode after different cycles.

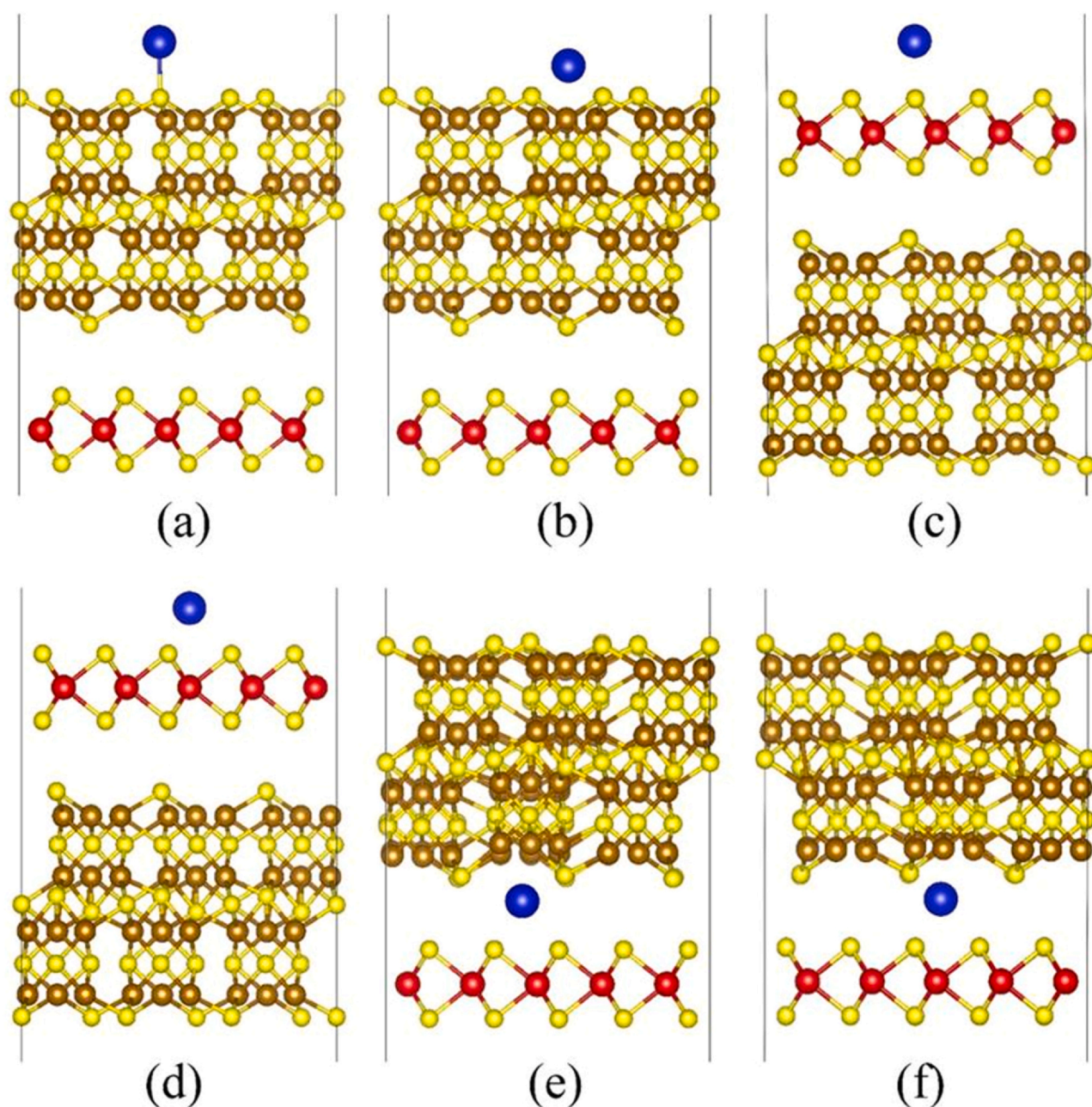


Fig. 8. The configurations of sodium into the FeS/MoS₂ hetero-bilayer. (a) Na adsorbed on the top of a S atom over FeS layer, (b) Na adsorbed on the top of a Fe atom over FeS layer, (c) Na adsorbed on the top of a S atom over MoS₂ layer, (d) Na adsorbed on the top of a Mo atom over MoS₂ layer, (e) Na adsorbed on the hollow site of the hexagon ring between MoS₂ and FeS layers, (f) Na adsorbed on the top of a Mo atom between FeS and MoS₂ layers.

For the FeS/MoS₂ composite, there are six typical positions for the adsorption of Na atom (Fig. 8). As illustrated in Table S1, the adsorption energies of Na atom in a, b, c, d, e and f are -2.91 , -3.72 , -2.10 , -2.36 , -3.87 and -4.22 eV, respectively. Previous simulation studies of Li⁺/Na⁺ batteries have shown that Li/Na atoms may be captured in the hetero-layers or on the surface of the electrode materials [79,80]. It is found that the adsorption energies of d and e sites are much lower than those of a, b, c and d, suggesting that Na atom tends to be adsorbed between MoS₂ and FeS layers in the FeS/MoS₂ hetero-bilayer. Moreover, the adsorption energy at e is 0.35 eV higher than that at f, which implies more Na atoms may be trapped on the top of Mo atom between FeS and MoS₂ layers.

The excellent electrochemical performance of FeS/MoS₂ composite is derived from the synergistic effects between FeS and MoS₂. The aggregation of MoS₂ is alleviated by an interfacial interaction

produced by van der Waals interaction between MoS₂ and FeS, which provides more active sites for electrode and electrolyte interaction. Owing to the improvement of the electron transfer efficiency under the interfacial interaction, the conductivity of FeS is enhanced. Meanwhile, the FeS/MoS₂ hetero-bilayer has the ability to improve the adsorption of sodium ions, which is conducive to the sodium storage in SIBs.

4. Conclusions

In summary, we have successfully compounded the MoS₂ onto the MIL-100(Fe) precursor via step by step process, producing the FeS/MoS₂ composite. This composite structure is beneficial to improve the electronic conductivity, alleviate the volume deformation of electrode, catch the polysulfide intermediate and increase specific

capacity. The band structure, electronic density of states (DOS) and adsorption energy are discussed by the density functional theory (DFT). Serving as anode for SIBs, FeS/MoS₂ manifests stable capacities of 464 and 365 mA h g⁻¹ at 0.1 and 1.0 A g⁻¹. The as-made material also delivers a good rate capability of 325 mA h g⁻¹ at a current density of 5.0 A g⁻¹, which are much better than those of FeS/FeS₂ and MoS₂. Even at a large current density of 2.0 A g⁻¹, it still delivers an excellent cycling capacity of 331 mA h g⁻¹. Such a heterostructure of MIL-100(Fe) composite 2D materials has broad application prospects in SIBs and is expected to expand to multivariate-MOF and covalent organic framework.

CRedit authorship contribution statement

Likang Fu: Conceptualization, Methodology, Data curation, Writing - original draft. **Wenqi Xiong:** Software, Validation, Writing - review & editing. **Qiming Liu:** Project administration, Funding acquisition. **Shuyun Wan:** Visualization, Investigation, Writing - review & editing. **Chenxia Kang:** Visualization, Investigation, Writing - review & editing. **Gaofeng Li:** Visualization, Investigation, Writing - review & editing. **Jun Chu:** Visualization, Investigation, Writing - review & editing. **Yucheng Chen:** Software, Validation, Writing - review & editing. **Shengjun Yuan:** Software, Validation, Writing - review & editing.

Declaration of Competing Interest

The authors declare that they have no known competing financial interests or personal relationships that could have appeared to influence the work reported in this paper.

Acknowledgements

This research was financially supported by the National Natural Science Foundation of China (51572202).

Appendix A. Supporting information

Supplementary data associated with this article can be found in the online version at doi:10.1016/j.jallcom.2021.159348.

References

- B. Dunn, H. Kamath, J.M. Tarascon, Electrical energy storage for the grid: a battery of choices, *Science* 334 (2011) 928–935.
- T. Tian, Z. Zeng, D. Vulpe, M.E. Casco, G. Divitini, P.A. Midgley, J. Silvestre-Albero, J.C. Tan, P.Z. Moghadam, D. Fairen-Jimenez, A sol-gel monolithic metal-organic framework with enhanced methane uptake, *Nat. Mater.* 17 (2018) 174–179.
- C. Liu, F. Li, L.P. Ma, H.M. Cheng, Advanced materials for energy storage, *Adv. Mater.* 22 (2010) E28–E62.
- J.B. Goodenough, Electrochemical energy storage in a sustainable modern society, *Energy Environ. Sci.* 7 (2014) 14–18.
- H. Ma, F. Cheng, J.Y. Chen, J.Z. Zhao, C.S. Li, Z.L. Tao, J. Liang, Nest-like silicon nanospheres for high-capacity lithium storage, *Adv. Mater.* 19 (2007) 4067–4070.
- J.B. Goodenough, Evolution of strategies for modern rechargeable batteries, *Acc. Chem. Res.* 46 (2013) 1053–1061.
- V. Palomares, P. Serras, I. Villaluenga, K.B. Hueso, J. Carretero-González, T. Rojo, Na-ion batteries, recent advances and present challenges to become low cost energy storage systems, *Energy Environ. Sci.* 5 (2012) 5884–5901.
- Y.V. Kaneti, J. Zhang, Y. He, Z. Wang, S. Tanaka, M.S.A. Hossain, Z. Pan, B. Xiang, Q. Yang, Y. Yamauchi, Fabrication of an MOF-derived heteroatom-doped Co/CoO/carbon hybrid with superior sodium storage performance for sodium-ion batteries, *J. Mater. Chem. A* 5 (2017) 15356–15366.
- Z. Shi, W. Kang, J. Xu, L. Sun, C. Wu, L. Wang, Y. Yu, D.Y. Yu, W. Zhang, C.S. Lee, In situ carbon-doped Mo(Se_{0.85}S_{0.15})₂ hierarchical nanotubes as stable anodes for high-performance sodium-ion batteries, *Small* 11 (2015) 5667–5674.
- J.Y. Hwang, S.T. Myung, Y.K. Sun, Sodium-ion batteries: present and future, *Chem. Soc. Rev.* 46 (2017) 3529–3614.
- P. He, X. Yu, X. Lou, Carbon-incorporated nickel-cobalt mixed metal phosphide nanoboxes with enhanced electrocatalytic activity for oxygen evolution, *Angew. Chem. Int. Ed.* 56 (2017) 3897–3900.
- Y. Wang, H. Fan, B. Hou, X. Rui, Q. Ning, Z. Cui, J. Guo, Y. Yang, X. Wu, Ni₁₅CoSe₅ nanocubes embedded in 3D dual N-doped carbon network as advanced anode material in sodium-ion full cells with superior low-temperature and high-power properties, *J. Mater. Chem. A* 6 (2018) 22966–22975.
- N. Yabuuchi, K. Kubota, M. Dahbi, S. Komaba, Research development on sodium-ion batteries, *Chem. Rev.* 114 (2014) 11636–11682.
- S. Hong, Y. Kim, Y. Park, A. Choi, N.S. Choi, K.T. Lee, Charge carriers in rechargeable batteries: Na ions vs. Li ions, *Energy Environ. Sci.* 6 (2013) 2067–2081.
- N. Yabuuchi, M. Kajiyama, J. Iwatate, H. Nishikawa, S. Hitomi, R. Okuyama, R. Usui, Y. Yamada, S. Komaba, P2-type Na_x[Fe_{1/2}Mn_{1/2}]O₂ made from earth-abundant elements for rechargeable Na batteries, *Nat. Mater.* 11 (2012) 512–517.
- D. Su, S. Dou, G. Wang, Ultrathin MoS₂ nanosheets as anode materials for sodium-ion batteries with superior performance, *Adv. Energy Mater.* 5 (2015) 1401205.
- J. Peng, J. Wang, H. Yi, W. Hu, Y. Yu, J. Yin, Y. Shen, Y. Liu, J. Luo, Y. Xu, A dual-insertion type sodium-ion full cell based on high-quality ternary-metal prussian blue analogs, *Adv. Energy Mater.* 8 (2018) 1702856.
- M. Okubo, C.H. Li, D.R. Talham, High rate sodium ion insertion into core-shell nanoparticles of Prussian blue analogues, *Chem. Commun.* 50 (2014) 1353–1355.
- L. Xiao, Y. Cao, J. Xiao, W. Wang, L. Kovarik, Z. Nie, J. Liu, High capacity, reversible alloying reactions in SnSb/C nanocomposites for Na-ion battery applications, *Chem. Commun.* 48 (2012) 3321–3323.
- Y. Zhao, A. Manthiram, High-capacity, high-rate Bi-Sb alloy anodes for lithium-ion and sodium-ion batteries, *Chem. Mater.* 27 (2015) 3106–3107.
- H. He, Q. Gan, H. Wang, G.L. Xu, X. Zhang, D. Huang, F. Fu, Y. Tang, K. Amine, M. Shao, Structure-dependent performance of TiO₂/C as anode material for Na-ion batteries, *Nano Energy* 44 (2018) 217–227.
- D. Yuan, X. Liang, L. Wu, Y. Cao, X. Ai, J. Feng, H. Yang, A honeycomb-layered Na₃Ni₂SbO₆: a high-rate and cycle-stable cathode for sodium-ion batteries, *Adv. Mater.* 26 (2014) 6301–6306.
- N. Voronina, H. Yashiro, S.T. Myung, Marcasite iron sulfide as a high-capacity electrode material for sodium storage, *J. Mater. Chem. A* 6 (2018) 17111–17119.
- Q. Lin, J. Zhang, D. Kong, T. Cao, S.W. Zhang, X. Chen, Y. Tao, W. Lv, F. Kang, Q.H. Yang, Deactivating defects in graphenes with Al₂O₃ nanoclusters to produce long-life and high-rate sodium-ion batteries, *Adv. Energy Mater.* 9 (2019) 1803078.
- H. Shuai, P. Ge, W. Hong, S. Li, J. Hu, H. Hou, G. Zou, X. Ji, Electrochemically exfoliated phosphorene-graphene hybrid for sodium-ion batteries, *Small Methods* 3 (2019) 1800328.
- M. Zhao, Z. Huang, S. Wang, L. Zhang, Y. Zhou, Design of l-cysteine functionalized UiO-66 MOFs for selective adsorption of Hg (II) in aqueous medium, *ACS Appl. Mater. Inter.* 11 (2019) 46973–46983.
- W. Xu, X. Pei, C.S. Diercks, H. Lyu, Z. Ji, O.M. Yaghi, A metal-organic framework of organic vertices and polyoxometalate linkers as a solid-state electrolyte, *J. Am. Chem. Soc.* 141 (2019) 17522–17526.
- M. Ding, R.W. Flaig, H. Jiang, O.M. Yaghi, Carbon capture and conversion using metal-organic frameworks and MOF-based materials, *Chem. Soc. Rev.* 48 (2019) 2783–2828.
- S. Bi, H. Banda, M. Chen, L. Niu, M. Chen, T. Wu, J. Wang, R. Wang, J. Feng, T. Chen, Molecular understanding of charge storage and charging dynamics in supercapacitors with MOF electrodes and ionic liquid electrolytes, *Nat. Mater.* 19 (2020) 552–558.
- J. Lee, O.K. Farha, J. Roberts, K.A. Scheidt, S.T. Nguyen, J.T. Hupp, Metal-organic framework materials as catalysts, *Chem. Soc. Rev.* 38 (2009) 1450–1459.
- S. Bai, X. Liu, K. Zhu, S. Wu, H. Zhou, Metal-organic framework-based separator for lithium-sulfur batteries, *Nat. Energy* 1 (2016) 1–6.
- K.Z. Elwakel, A. Shahat, Z.A. Khan, W. Alshitari, E. Guibal, Magnetic metal oxide-organic framework material for ultrasonic-assisted sorption of Titan Yellow and Rose Bengal from aqueous solutions, *Chem. Eng. J.* 392 (2020) 123635.
- X. Yu, Y. Feng, Y. Jeon, B. Guan, X. Lou, U. Paik, Formation of Ni-Co-MoS₂ nanoboxes with enhanced electrocatalytic activity for hydrogen evolution, *Adv. Mater.* 28 (2016) 9006–9011.
- K. Jayaramulu, D.P. Dubal, A. Schneemann, V. Ranc, C. Perez-Reyes, J. Stráská, Š. Kment, M. Otyepka, R.A. Fischer, R. Zboril, Shape-assisted 2D MOF/graphene derived hybrids as exceptional lithium-ion battery electrodes, *Adv. Funct. Mater.* 29 (2019) 1902539.
- X. Zhang, W. Qin, D. Li, D. Yan, B. Hu, Z. Sun, L. Pan, Metal-organic framework derived porous CuO/Cu₂O composite hollow octahedrons as high performance anode materials for sodium ion batteries, *Chem. Commun.* 51 (2015) 16413–16416.
- K. Xu, Q. Pan, F. Zheng, G. Zhong, C. Wang, S. Wu, C. Yang, Hierarchical nitrogen-doped porous carbon microspheres as anode for high performance sodium ion batteries, *Front. Chem.* 7 (2019) 733.
- X. Liu, F. Zou, K. Liu, Z. Qiang, C.J. Taubert, P. Ustriyana, B.D. Vogt, Y. Zhu, A binary metal organic framework derived hierarchical hollow Ni₃S₂/Co₉S₈/N-doped carbon composite with superior sodium storage performance, *J. Mater. Chem. A* 5 (2017) 11781–11787.
- W. Gang, Z. Jian, Y. Sheng, F. Wang, X. Feng, Vertically aligned MoS₂ nanosheets patterned on electrochemically exfoliated graphene for high performance lithium and sodium storage, *Adv. Energy Mater.* 8 (2018) 1702254.
- Z. Shi, W. Kang, J. Xu, Y. Sun, M. Jiang, T.W. Ng, H. Xue, D.Y.W. Yu, W. Zhang, C.S. Lee, Hierarchical nanotubes assembled from MoS₂-carbon monolayer sandwiched superstructure nanosheets for high-performance sodium ion batteries, *Nano Energy* 22 (2016) 27–37.

- [40] G. Li, D. Luo, X. Wang, M.H. Seo, S. Hemmati, A. Yu, Z. Chen, Enhanced reversible sodium-ion intercalation by synergistic coupling of few-layered MoS₂ and S-doped graphene, *Adv. Funct. Mater.* 27 (2017) 1702562.
- [41] S. Dan, D. Ye, L. Ping, Y. Tang, H. Wang, MoS₂/graphene nanosheets from commercial bulky MoS₂ and graphite as anode materials for high rate sodium-ion batteries, *Adv. Energy Mater.* 8 (2017) 1702383.
- [42] I. Bezverkhy, E. Popova, N. Geoffroy, F. Herbst, J.P. Bellat, Preparation of magnetic composites of MIL-53(Fe) or MIL-100(Fe) via partial transformation of their framework into γ -Fe₂O₃, *J. Mater. Chem. A* 4 (2016) 8141–8148.
- [43] Y. Wang, W. Kang, D. Cao, M. Zhang, Z. Kang, Z. Xiao, R. Wang, D. Sun, A yolk-shelled Co₉S₈/MoS₂-CN nanocomposite derived from a metal-organic framework as a high performance anode for sodium ion batteries, *J. Mater. Chem. A* 6 (2018) 4776–4782.
- [44] J.P. Perdew, K. Burke, M. Ernzerhof, Generalized gradient approximation made simple, *Phys. Rev. Lett.* 77 (1996) 3865–3868.
- [45] J. Hendrik, M. James, D. Pack, Special points for Brillouin-zone integrations, *Phys. Rev. B* 13 (1976) 12–15.
- [46] S. Grimme, Semiempirical GGA-type density functional constructed with a long-range dispersion correction, *J. Comput. Chem.* 27 (2010) 1787–1799.
- [47] J. Sauer, M. Sierka, Combining quantum mechanics and interatomic potential functions in ab initio studies of extended systems, *J. Comput. Chem.* 21 (2000) 1470–1493.
- [48] D. Li, Y. Sun, S. Chen, J. Yao, Y. Zhang, Y. Xia, D. Yang, Highly porous FeS/carbon fibers derived from Fe-carrageenan biomass: high-capacity and durable anodes for sodium-ion batteries, *ACS Appl. Mater. Inter.* 10 (2018) 17175–17182.
- [49] Y. Wang, J. Yang, S. Chou, H. Liu, W. Zhang, D. Zhao, S. Dou, Uniform yolk-shell iron sulfide-carbon nanospheres for superior sodium-iron sulfide batteries, *Nat. Commun.* 6 (2015) 1–9.
- [50] T. Yamashita, P. Hayes, Analysis of XPS spectra of Fe²⁺ and Fe³⁺ ions in oxide materials, *Appl. Surf. Sci.* 254 (2008) 2441–2449.
- [51] X. Fan, P. Xu, D. Zhou, Y. Sun, T.E. Mallouk, Fast and efficient preparation of exfoliated 2H MoS₂ nanosheets by sonication-assisted lithium intercalation and infrared laser-induced 1T to 2H phase reversion, *Nano Lett.* 15 (2015) 5956–5960.
- [52] J. Wang, C. Luo, T. Gao, A. Langrock, C. Wang, An advanced MoS₂/carbon anode for high-performance sodium-ion batteries, *Small* 11 (2015) 473–481.
- [53] M.A. Baker, R. Gilmore, C. Lenardi, W. Gissler, XPS investigation of preferential sputtering of S from MoS₂ and determination of MoS_x stoichiometry from Mo and S peak positions, *Appl. Surf. Sci.* 150 (1999) 255–262.
- [54] L. Lai, G. Huang, X. Wang, J. Weng, Solvothermal syntheses of hollow carbon microspheres modified with -NH₂ and -OH groups in one-step process, *Carbon* 48 (2010) 3145–3156.
- [55] A.E. Shalagina, Z.R. Ismagilov, O.Y. Podyacheva, R.I. Kvon, V.A. Ushakov, Synthesis of nitrogen-containing carbon nanofibers by catalytic decomposition of ethylene/ammonia mixture, *Carbon* 45 (2007) 1808–1820.
- [56] T. Zhang, Y. Feng, J. Zhang, C. He, J. Song, Ultrahigh-rate sodium-ion battery anode enabled by vertically aligned (1T–2H MoS₂)/CoS₂ hetero-nanosheets, *Mater. Today Nano* 12 (2020) 10089.
- [57] X. Zhu, N.R. Monahan, Z. Gong, H. Zhu, K.W. Williams, C.A. Nelson, Charge transfer excitons at van der Waals interfaces, *J. Am. Chem. Soc.* 137 (2015) 8313–8320.
- [58] C. Huang, S. Wu, A.M. Sanchez, J.J.P. Peters, R. Beanland, J.S. Ross, P. Rivera, W. Yao, D.H. Cobden, X. Xu, Lateral heterojunctions within monolayer semiconductors, *Nat. Mater.* 13 (2014) 1096–1101.
- [59] J. Diao, Y. Qiu, S. Liu, W. Wang, X. Guo, Interfacial engineering of W₂N/WC heterostructures derived from solid-state synthesis: a highly efficient trifunctional electrocatalyst for ORR, OER, and HER, *Adv. Mater.* 32 (2020) 1905679.
- [60] C. Xu, Y. Zeng, X. Rui, N. Xiao, J. Zhu, W. Zhang, J. Chen, W. Liu, H. Tan, H.H. Hng, Controlled soft-template synthesis of ultrathin C@FeS nanosheets with high-Li-storage performance, *ACS Nano* 6 (2012) 4713–4721.
- [61] J. Wang, J. Liu, H. Yang, D. Chao, J. Yan, S.V. Savilov, J. Lin, Z. Shen, MoS₂ nanosheets decorated Ni₃S₂@MoS₂ coaxial nanofibers: constructing an ideal heterostructure for enhanced Na-ion storage, *Nano Energy* 20 (2016) 1–10.
- [62] F. Zhou, S. Xin, H. Liang, L. Song, S. Yu, Carbon nanofibers decorated with molybdenum disulfide nanosheets: synergistic lithium storage and enhanced electrochemical performance, *Angew. Chem. Int. Ed.* 53 (2014) 11552–11556.
- [63] T. Shan, S. Xin, Y. You, H. Cong, S. Yu, A. Manthiram, Combining nitrogen-doped graphene sheets and MoS₂: a unique film-foam-film structure for enhanced lithium storage, *Angew. Chem. Int. Ed.* 55 (2016) 12783–12788.
- [64] Q. Wang, W. Zhang, C. Guo, Y. Liu, C. Wang, Z. Guo, In situ construction of 3D interconnected FeS@Fe₃C/graphitic carbon networks for high-performance sodium-ion batteries, *Adv. Funct. Mater.* 27 (2017) 1703390.
- [65] L. Fei, Q. Lin, B. Yuan, G. Chen, P. Xie, Y. Li, Y. Xu, S. Deng, S. Smirnov, H. Luo, Reduced graphene oxide wrapped FeS nanocomposite for lithium-ion battery anode with improved performance, *ACS Appl. Mater. Inter.* 5 (2013) 5330–5335.
- [66] D. Zhang, J.P. Tu, J.Y. Xiang, Y.Q. Qiao, X.H. Xia, X.L. Wang, C.D. Gu, Influence of particle size on electrochemical performances of pyrite FeS₂ for Li-ion batteries, *Electrochim. Acta* 56 (2011) 9980–9985.
- [67] Z. Hu, K. Zhang, Z. Zhu, Z. Tao, J. Chen, FeS₂ microspheres with an ether-based electrolyte for high-performance rechargeable lithium batteries, *J. Mater. Chem. A* 3 (2015) 12898–12904.
- [68] H. Li, Y. Su, W. Sun, Y. Wang, Carbon nanotubes rooted in porous ternary metal sulfide@N/S-doped carbon dodecahedron: bimetal-organic-frameworks derivation and electrochemical application for high-capacity and long-life lithium-ion batteries, *Adv. Funct. Mater.* 26 (2016) 8345–8353.
- [69] X. Xu, D. Yu, H. Zhou, L. Zhang, C. Xiao, C. Guo, S. Guo, S. Ding, MoS₂ nanosheets grown on amorphous carbon nanotubes for enhanced sodium storage, *J. Mater. Chem. A* 4 (2016) 4375–4379.
- [70] W. Kang, Y. Wang, J. Xu, Recent progress in layered metal dichalcogenide nanostructures as electrodes for high-performance sodium-ion batteries, *J. Mater. Chem. A* 5 (2017) 7767–7790.
- [71] J.Y. Liao, B.D. Luna, A. Manthiram, TiO₂-B nanowire arrays coated with layered MoS₂ nanosheets for lithium and sodium storage, *J. Mater. Chem. A* 4 (2016) 801–806.
- [72] Z. Wu, J. Li, Y. Zhong, J. Liu, K. Wang, X. Guo, L. Huang, B. Zhong, S. Sun, Synthesis of FeS@C-N hierarchical porous microspheres for the applications in lithium/sodium ion batteries, *J. Alloy. Compd.* 688 (2016) 790–797.
- [73] D. Xie, S. Cai, X. Sun, T. Hou, Y. Lin, FeS/ZnS nanoflower composites as high performance anode materials for sodium ion batteries, *Inorg. Chem. Commun.* 111 (2020) 107635.
- [74] Z. Cao, H. Song, B. Cao, J. Ma, X. Chen, J. Zhou, Z. Ma, Sheet-on-sheet chrysanthemum-like C/FeS microspheres synthesized by one-step solvothermal method for high-performance sodium-ion batteries, *J. Power Sources* 364 (2017) 208–214.
- [75] K. Yao, Z. Xu, Z. Li, X. Liu, X. Shen, L. Cao, J. Huang, Synthesis of grain-like MoS₂ for high-performance sodium-ion batteries, *ChemSusChem* 11 (2018) 2130–2137.
- [76] Y. Cai, H. Yang, J. Zhou, Z. Luo, G. Fang, S. Liu, A. Pan, S. Liang, Nitrogen doped hollow MoS₂/C nanospheres as anode for long-life sodium-ion batteries, *Chem. Eng. J.* 327 (2017) 522–529.
- [77] L. Wang, C. Wang, N. Zhang, F. Li, F. Cheng, J. Chen, High anode performance of in situ formed Cu₂Sb nanoparticles integrated on Cu foil via replacement reaction for sodium-ion batteries, *ACS Energy Lett.* 2 (2016) 256–262.
- [78] Q. Chen, S. Sun, T. Zhai, M. Yang, X. Zhao, H. Xia, Yolk-shell NiS₂ nanoparticle-embedded carbon fibers for flexible fiber-shaped sodium battery, *Adv. Energy Mater.* 8 (2018) 1800054.
- [79] X. Xie, Z. Ao, D. Su, J. Zhang, G. Wang, MoS₂/graphene composite anodes with enhanced performance for sodium-ion batteries: the role of the two-dimensional heterointerface, *Adv. Funct. Mater.* 25 (2015) 1393–1403.
- [80] R.H. Miwa, W.L. Scopel, Lithium incorporation at the MoS₂/graphene interface: an ab initio investigation, *J. Phys. Condens. Matter* 25 (2013) 445301.